Fluid driven shear cracks on a strengthening rate-and-state frictional fault

Pierre Dublanchet

▶ **To cite this version:**

Pierre Dublanchet. Fluid driven shear cracks on a strengthening rate-and-state frictional fault. Journal of the Mechanics and Physics of Solids, 2019, 132, pp.103672. 10.1016/j.jmps.2019.07.015 . hal-02367634

HAL Id: hal-02367634
https://hal.science/hal-02367634

Submitted on 20 Dec 2021

HAL is a multi-disciplinary open access archive for the deposit and dissemination of scientific research documents, whether they are published or not. The documents may come from teaching and research institutions in France or abroad, or from public or private research centers.

L'archive ouverte pluridisciplinaire **HAL**, est destinée au dépôt et à la diffusion de documents scientifiques de niveau recherche, publiés ou non, émanant des établissements d'enseignement et de recherche français ou étrangers, des laboratoires publics ou privés.

Distributed under a Creative Commons Attribution - NonCommercial 4.0 International License

Version of Record: https://www.sciencedirect.com/science/article/pii/S0022509619305393
Manuscript_2cdece177b383331c9bb4ec31c461500

Fluid driven shear cracks on a strengthening rate-and-state frictional fault

P. Dublanchet[a]

[a] *MINES ParisTech, PSL Research University, Centre de Géosciences, 35 rue saint-honoré 77305 Fontainebleau, France*

Abstract

This study is dedicated to the dynamics of slow slip (or creep) reactivation on faults stimulated by a fluid injection. Fluid driven slow slip events involving slip rates too small to generate detectable elastic waves (typically less than 1 cm.s^{-1}) are commonly observed on natural faults either in tectonic active areas or in the framework of deep energy exploitation. We model the fault as a planar 2D velocity strengthening rate-and-state frictional interface embedded in an elastic medium. The fluid is injected at a constant rate and spreads diffusively along the fault reducing the effective normal stress. We show that the fluid injection initiates a shear crack on the fault. In a first phase, the shear crack remains confined to the pressurized zone, and slip-rate increases exponentially with time. A second phase starts at the onset of a rapid crack expansion. The shear crack during phase two expands faster than the pressurized zone. Depending on the prestress conditions, the shear crack evolves towards two different regimes. If the initial shear stress τ_0 is larger than the steady-state residual frictional stress τ_r within the crack, the slip rate and the crack expansion rate blow up in a finite time. This accelerating crack regime is similar to the nucleation of a dynamic rupture on the fault. On the other hand, if $\tau_0 < \tau_r$, the accelerated expansion progressively slows down so that the crack enters a steady regime, characterized by a constant expansion speed and a logarithmic increase of slip-rate. However, a large majority of fault scenarios ultimately lead to this steady expansion regime, which is also the most probable scenario on real tectonic faults. In addition to the numerical results, we develop asymptotic expressions for the the maximum

© 2019 published by Elsevier. This manuscript is made available under the CC BY NC user license
https://creativecommons.org/licenses/by-nc/4.0/

slip rate history on the fault and the crack length history, showing how initial prestress τ_0, frictional conditions (ratio a/b), hydraulic properties and injection history control the dynamics of fluid induced aseismic slip events.

Keywords: Strengthening and mechanisms (A), Friction (B), Geological materials (B), Crack mechanics (B)

1. Introduction

Many observations suggest that fluid flow at depth can reactivate slip on preexisting crustal faults. Fluids may have a natural origin (rainfall events (Hainzl et al., 2006), deep source (Duverger et al., 2015), volcanic activity (Ágústsdóttir et al., 2016)) or can be related to geo-resource exploitation (geothermal operations (Deichmann and Giardini, 2009), waste water injection (Ellsworth, 2013), reservoir lake impoundement (Gupta et al., 1969)). If rapid enough slip is reactivated (typically at slip rates greater than 1 cm.s^{-1} which allows the radiation of detectable elastic waves), the fault ruptures in an earthquake, such as the commonly observed induced earthquakes (Deichmann and Giardini, 2009; Ellsworth, 2013). However, the fluid-induced reactivation of faults can lead to much slower slip speeds, leading to the occurrence of a slow slip event (Cornet et al., 1997; Cornet, 2016; Guglielmi et al., 2015). Such slow slip events are also refered as accelerated creep, or aseismic events. Aseismic slip in turn may trigger earthquake sequences (Schaff et al., 1998; Bourouis and Bernard, 2007; Wei et al., 2015; Lengliné et al., 2017). Aseismic slip is even suspected to be one of the dominant mechanisms releasing injected energy in the context of fluid operations at depth (Goodfellow et al., 2015; Duboeuf et al., 2017). Understanding the physics controlling the dynamics of aseismic slip events triggered by fluid injections is therefore crucial to better constrain the energy partitioning in the subsurface or in a geological reservoir, and to better assess the associated seismogenic hazard.

Recent advances in the study of the mechanics of fluid-fault interaction have essentially focused on the stability of frictional slip when a fluid is lo-

cally injected and diffuses within a fault (Garagash and Germanovich, 2012; Cappa et al., 2018; Bhattacharya and Viesca, 2019), or when a hydraulic fracture propagates along a frictional fault (Azad et al., 2017). All these studies have shown how the pore pressure related reduction in effective normal stress triggers the reactivation of a slow aseismic slip, that eventually degenerates into a dynamic rupture. In most of the fault scenarios investigated, the aseismic slip (and the dynamic slip if initiated) is excited well beyond the pressurized region of the fault. This strong aseismic response (stronger that the pore pressure perturbation) is even more pronounced when the fault experiences significant frictional weakening (Garagash and Germanovich, 2012; Azad et al., 2017; Cappa et al., 2018), or if slip-induced permeability enhancement takes place (Cappa et al., 2018; Bhattacharya and Viesca, 2019). The transition to dynamic rupture is furthermore facilitated by initial stress conditions closer to failure, and by an injection scenario leading to an abrupt increase of over-pressure within the fault zone (Garagash and Germanovich, 2012; Azad et al., 2017).

All these studies rely on a frictional description involving either a constant friction coefficient or a slip weakening friction coefficient. Such descriptions impose a minimum over-pressure to trigger slow slip. Below this reactivation threshold, no slip occurs. Furthermore, the slip-rate dependence of friction needed to explain the dynamics of aseismic slip on tectonic faults (Marone et al., 1991; Perfettini and Avouac, 2004; Helmstetter and Shaw, 2009; Jolivet et al., 2013) is not accounted for by such frictional models. A long history of rock friction experiments has demonstrated that the rate-and-state friction (Dieterich, 1979; Ruina, 1983) captures both the slip-rate and the slip history dependence of friction. Contrary to the slip weakening description, the rate-and-state law does not impose a stress threshold to activate slip, which may lead to a fairly different behavior than what has been obtained under slip weakening or constant friction. This point still needs to be investigated. A rate-and-state friction coefficient has however been tested by Cappa et al. (2018) to model the in-situ fault reactivation experiment by Guglielmi et al. (2015), leading to a somewhat larger slow slip response than predicted by the classical constant friction coeffi-

cient. However, more efforts still need to be done to understand the effects of the rate-and-state frictional rheology on fluid induced aseismic slip.

Here we propose to study the fluid induced reactivation of aseismic slip on a Dieterich-Ruina rate-and-state frictional fault. We will extend the previous studies on fluid fault interaction by studying, for a prescribed injection and fluid flow scenario, the effect of the rate-and-state parameters and the initial stress conditions on the induced aseismic slip. In particular, we will focus on the evolution of maximum slip rate and the size of the perturbed slip zone as the pore pressure perturbation proceeds. As far as possible we will derive closed form approximate solutions for the maximum slip rate history and for the size evolution of the aseismic slow slip events.

2. Fault model

We consider the anti-plane fault model depicted in figure 1, consisting in a linear 1D interface separating two 2D semi-infinite elastic media. The fault is loaded by a constant normal stress σ, and a remote shear stress τ_0. Anti-plane slip - $\delta(x,y,t) = w(x,0^+,t) - w(x,0^-,t)$, w being the z component of the displacement, and t the elaspsed time - is resisted by friction within a finite length crack of size $2L_0$. Outside the crack, the slip-rate is imposed at a constant rate $v*$. Here we consider rate-and-state friction within the crack, which accounts for the slip rate and slip history dependence of friction usually observed in laboratory experiments (Dieterich, 1979; Marone, 1998). The fault is furthermore permeated by a fluid injected at $x = 0$, and diffusing in the $\pm x$ directions with pore pressure p. In this framework, the frictional stress along the x direction τ is given by :

$$\tau(x,t) = f(x,t)\left[\sigma - p(x,t)\right], \tag{1}$$

f being the rate-and-state friction coefficient defined as :

$$f(x,t) = f_0 + a\ln\frac{v(x,t)}{v*} + b\ln\frac{\theta(x,t)v*}{d_c}, \tag{2}$$

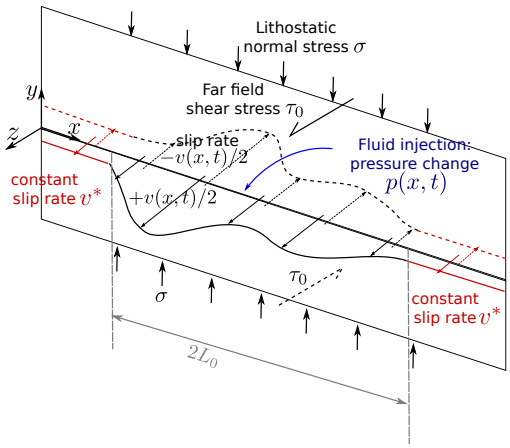

Figure 1: 2D mode III fault model considered in this study.

where f_0 is a constant friction coefficient, a and b are rate-and-state parameters, d_c the critical slip of rate-and-state friction needed to renew a population of microscopic contacts. v is the slip rate defined as $v = \dot{\delta}$. The state variable θ incorporates the slip history dependence of the friction coefficient. Here it is assumed to evolve with time and slip rate on the fault according to the ageing law (Ruina, 1983; Marone, 1998) :

$$\dot{\theta}(x,t) = 1 - \frac{v(x,t)\theta(x,t)}{d_c}. \tag{3}$$

The steady-state friction coefficient f_{ss} at the slip rate v is obtained when $\dot{\theta} = 0$, so that $\theta = d_c/v$ from equation (3). We get:

$$f_{ss} = f_0 + (a-b)\ln\frac{v}{v*}. \tag{4}$$

The steady-state frictional stress τ_{ss} is then defined as $\tau_{ss} = f_{ss}(\sigma - p)$. Since we are interested in the dynamics of slow aseismic slip, rate strengthening properties are considered so that $a > b$ and the steady state shear stress is an increasing function of slip rate. Assuming velocity strengthening properties prevents the development of spontaneous slip instabilities (Ruina, 1983; Rubin and Ampuero, 2005), or stick slip oscillations on the fault, and rather al-

lows the fault to undergo stable creep at $v = v^*$ in the absence of pore pressure perturbation. Following Rubin and Ampuero (2005), we note $\Omega = v\theta/d_c$ the distance to steady state, since $f - f_{ss} = \ln \Omega$.

We further assume that the slip distribution on the fault results from a balance between the frictional stress τ (equation 1) and the z component of the elastostatic stress $\tau_{el} = \tau_{yz}(x, 0, t) = \mu \partial w / \partial y(x, 0, t)$. τ_{el} could be written as :

$$\tau_{el}(x,t) = \tau_0(x) - \frac{\mu}{2}\mathcal{H}\left[\delta'\right](x,t), \tag{5}$$

where τ_0 corresponds to the initial prestress, that is the stress prevailing on the fault before the onset of slip. The second term on the right-hand side is the static shear stress generated by the slip distribution δ. The operator $\mathcal{H}$ is the Hilbert transform, and the prime denotes a derivative with respect to the spatial coordinate x.

The fluid injection is modeled as a prescribed pore pressure history resulting from a constant injection rate imposed at $x = 0$, and a diffusion along the infinite x axis with a constant diffusivity D. Under such conditions, the pore pressure history p is given by (see Turcotte and Schubert (2014) for details of the derivation):

$$p(x,t) = 2q\sqrt{Dt}\left[|\eta|(erf(|\eta|) - 1) + \frac{e^{-\eta^2}}{\sqrt{\pi}}\right], \tag{6}$$

where the similarity variable η is defined as $\eta = x/2\sqrt{Dt}$ and q is the change in pressure gradient (directly related to the fluid flux according to the Darcy's law) at the origin.

The time derivative of the quasi-static stress balance $\tau = \tau_{el}$, along with the state evolution law (3) leads to the following differential equations for the evolution of slip rate v and state variable θ under prescribed pore pressure

history p:

$$\begin{cases} (\sigma - p)\left[a\dfrac{\dot{v}}{v} + b\dfrac{\dot{\theta}}{\theta}\right] = f(v,\theta)\dot{p} - \dfrac{\mu}{2}\mathcal{H}\left[v'\right] \\ \dot{\theta} = 1 - \dfrac{v\theta}{d_c}. \end{cases} \tag{7}$$

Considering a characteristic slip rate $v_c = v*$, a characteristic time $t_c = d_c/v*$, a characteristic length $x_c = \mu d_c/b\sigma$, and a characteristic pore pressure $p_c = \sigma$, we can make the substitution:

$$v \Rightarrow v/v_c, \qquad t \Rightarrow t/t_c, \qquad x \Rightarrow x/x_c, \qquad p \Rightarrow p/p_c, \tag{8}$$

so that the system (7) becomes in non-dimensional form:

$$\begin{cases} (1-p)\left[\alpha\dfrac{\dot{v}}{v} + \dfrac{\dot{\theta}}{\theta}\right] = \bar{f}(v,\theta)\dot{p} - \dfrac{1}{2}\mathcal{H}\left[v'\right] \\ \dot{\theta} = 1 - v\theta, \end{cases} \tag{9}$$

where $\alpha = a/b$ and $\bar{f} = \bar{f}_0 + \alpha \ln v + \ln\theta$, $\bar{f}_0$ corresponding to f_0/b. Similarly, the frictional stress τ and the steady-state frictional stress τ_{ss} could be made non dimensional and become:

$$\begin{cases} \tau = \left[\bar{f}_0 + \alpha \ln v + \ln\theta\right](1-p) \\ \tau_{ss} = \left[\bar{f}_0 + (\alpha - 1)\ln v\right](1-p) \end{cases} \tag{10}$$

Finally, the pore pressure history (6) could be made non-dimensional. From the characteristic lenth x_c the characteristic time t_c, and the characteristic pore pressure p_c, we construct the characteristic diffusivity $D_c = x_c^2/t_c = \mu^2 d_c v * /b^2\sigma^2$, and the characteristic pore pressure gradient $q_c = p_c/x_c = b\sigma^2/\mu d_c$. Assuming the substitution

$$D \Rightarrow D/D_c, \qquad q \Rightarrow q/q_c, \tag{11}$$

along with (8), the non-dimensional pore pressure history keeps the form (6).

In order to simplify the developments in the main text, we will in the following make only use of non-dimensional quantities removing the over-bar on

f and f_0. However, the figures will be labeled with dimensional quantities, so that the relevant physical parameters appear more explicitly. A length L in the main text will therefore correspond to the non-dimensional $\bar{L} = Lb\sigma/\mu d_c$, but not in the figure label.

For a specific choice of the parameters α, q, D, and initial conditions $v(x,0) = v_0(x)$, $\theta(x,0) = \theta_0(x)$ the system (9) is solved numerically using a standard Runge-Kutta Fehlberg scheme (Fehlberg, 1969) with adaptative time stepping as detailed by Dublanchet (2017). This requires to evaluate the Hilbert transform of the slip rate gradient at each time step. For that we follow the method proposed by Cochard and Rice (1997), on a grid of $n = 8192$ identical computational cells of normalized size $h = 0.03$ much smaller than the typical normalized process zone size $L_b = 1$ (Perfettini and Ampuero, 2008; Rubin and Ampuero, 2005) in order to ensure continuity. This algorithm results in the slip rate and state variable history $v(x,t)$ and $\theta(x,t)$, in response to a fluid injection.

3. Results

We performed several fluid injection tests at constant rate in our fault model. In each scenario, we considered a normalized diffusivity $D = 4.369$, which corresponds to hydraulic diffusivities ranging between 10^{-6} m^2.s^{-1} and 0.1 m^2.s^{-1} assuming standard values for the shear modulus $\mu \sim 3.10^{10}$ Pa, for the rate-and-state parameter $b \sim 10^{-3} - 10^{-2}$, for the reference creep rate $v* = 10^{-9} - 10^{-10}$ m.s^{-1} (representative of creeping faults), for the lithostatic stress $\sigma \sim 100$ MPa (representative of approximately 3 km depth) and the critical slip distance d_c between 1 mm and 1 μm (Marone, 1998). Typical diffusivities within fault gouge are expected to vary within this range (Rice, 2006; Jaeger et al., 2009). We considered a constant normalized pore pressure gradient at the origin $q = 0.01$, which corresponds to a pressure gradient of the order of 300 Pa.m^{-1} to 100 MPa.m^{-1} with the same reference parameters. We assumed a normalized reference friction coefficient $f_0 = 600$, which corresponds to a non normalized value of 0.6 with $b = 10^{-3}$ in agreement with laboratory experiments (Marone, 1998).

We tested 8 values of the velocity strengthening frictional parameter α between 1.1 (weakly strengthening behavior) to 2.5 (strongly strengthening behavior).

All the injection scenarios were performed on a fault initially slipping at the uniform background slip rate $v_0 = 1$. For all the frictional parameters, we considered three different uniform initial state variable $\theta_0 = 1, e^2$ and e^{-2}, so that the initial stress $\tau_0 = f_0 + \alpha \ln v_0 + \ln \theta_0$ on the fault is respectively equal to, slightly above or slightly below steady state at $v = 1$ from equations (10). The three initial stress conditions indeed correspond to $\tau_0 - \tau_{ss}^0 = 0, 2$ or -2, τ_{ss}^0 being the steady state frictional stress at the reference slip rate $v = 1$, and with $p = 0$. Although we expect stable creeping faults to be at steady-state, they may undergo stress perturbations associated with the occurence of earthquakes in their vicinity, especially in tectonic active environments. Stress perturbations lead to transient deviations from the steady-state stress that can survive for a few hours to a few years, as suggested by the observations of post-seismic accelerated creep (Helmstetter and Shaw, 2009). Creeping faults may therefore be not exactly at steady-state at the time of an injection. For that reason we not only consider initial conditions at steady state.

All the simulations were stopped before the maximum pore pressure exceeds the lithostatic normal stress $\sigma = 1$, so that no mode I hydraulic fracture is created (which implies a loss of frictional contact, so that the model used here is no longer valid).

Two characteristic slip responses to a fluid injection are illustrated in figure 2: as the pore pressure perturbation develops, slip accelerates on a patch centered on the injection point (figures 2(a) and (b)). Within the slipping patch, the initial stress is reduced, and redistributed on the non perturbed remote portions of the fault (figures 2(c) and (d)). The fluid injection therefore initiates the development of a shear crack on the fault. Note that in both examples, the maximum slip rate is amplified by up to a factor 10^5, which is typically in the range of slow aseismic slip (or creep) if we assume a reference slip rate of 10^{-9} m.s^{-1}. As this will be discussed later, two mechanisms drive the development of this crack: the reduction of effective normal stress due to the presence of fluid,

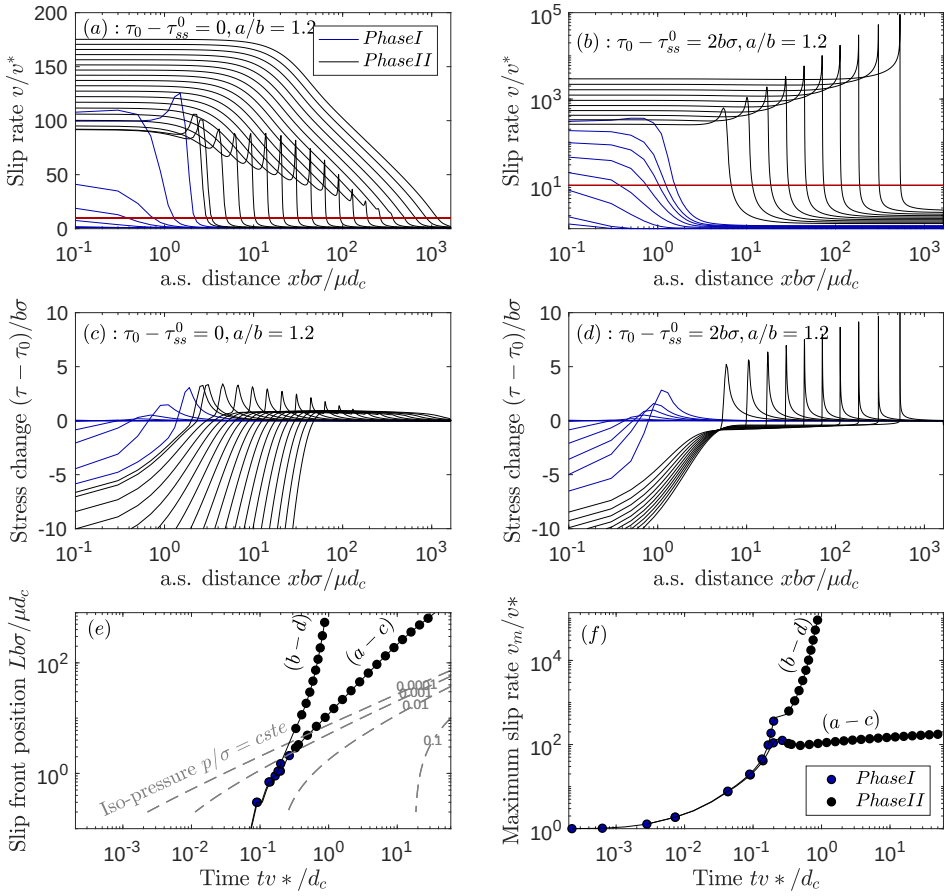

Figure 2: Two examples of fluid driven fault slip reactivation: fault initially at steady state (a,c), and initially above steady state (b,d).(a,b): Normalized slip rate. (c,d): Normalized shear stress change. τ_0 is the initial stress on the fault before the injection, and τ_{ss}^0 the steady-state frictional stress at the reference slip rate v^* and pore pressure $p = 0$. The profiles being symmetric around $x = 0$, only the right half profiles are represented. a.s. refers to along strike. (e): Slipping patch normalized half-length (or slip front position), defined as the size of the patch where slip rate exceeds the red line in figures (a,b). Gray dotted lines indicate iso-pressure levels. The grey numbers are levels of normalized pore pressure. (f): Maximum normalized slip rate. Each dot in (e,f) corresponds to a profile in figures (a,b,c,d). Blue lines and symbols correspond to phase I of slip reactivation, black lines and symbols correspond to the second phase of slip reactivation (see main text for details).

or the initial prestress.

We observe two successive phases in the evolution of such a pressurized crack: at the very beginning of the injection (phase I), the crack is confined to the central region of the fault, but rapidly, it starts to expand along strike (phase II). During phase I, the maximum slip rate on the crack increases exponentially with time from injection start. As illustrated in figure 2, we get a different behavior during phase II for different initial stress conditions: for a fault initially at steady state, the crack expansion occurs approximately at a constant rupture speed (figure 2(a,c,e)), and the maximum slip rate increases logarithmically in time (figure 2(f)). For a fault initially above steady state, both the crack length and the maximum slip rate blow up in a finite time (figure 2(b,d,e,f)). In the following we will refer to these two modes as the steady crack (constant rupture speed), or the accelerating crack (diverging slip rate).

The half crack length $L(t)$ and the maximum slip rate $v_m(t)$ histories for all the fault scenarios investigated are shown in figure 3. Here again, maximum slip rates remain within the range of what is typically called aseismic slow slip. As illustrated in figure 2, $L(t)$ is defined as the half length of the patch experiencing more than a 10 times increase in slip rate. From figure 3, $L(t)$ and $v_m(t)$ are both influenced by the frictional conditions α and by the initial state of stress. Interestingly, neither the steady nor the accelerating crack follows an iso-pressure path: the crack dynamics is not directly controlled by the pore pressure diffusion. In all the scenarios the crack propagates faster than the pressurized zone does. However, all the results lead either to the steady crack, or to the accelerating crack. The latter fault response is typically obtained for a α parameter close to the weakening transition (i.e. for α close to 1), and for a fault initially stressed above steady state.

In the following, we will study the details of slip rate acceleration during phase I, the transition to phase II, and the crack expansion during phase II.

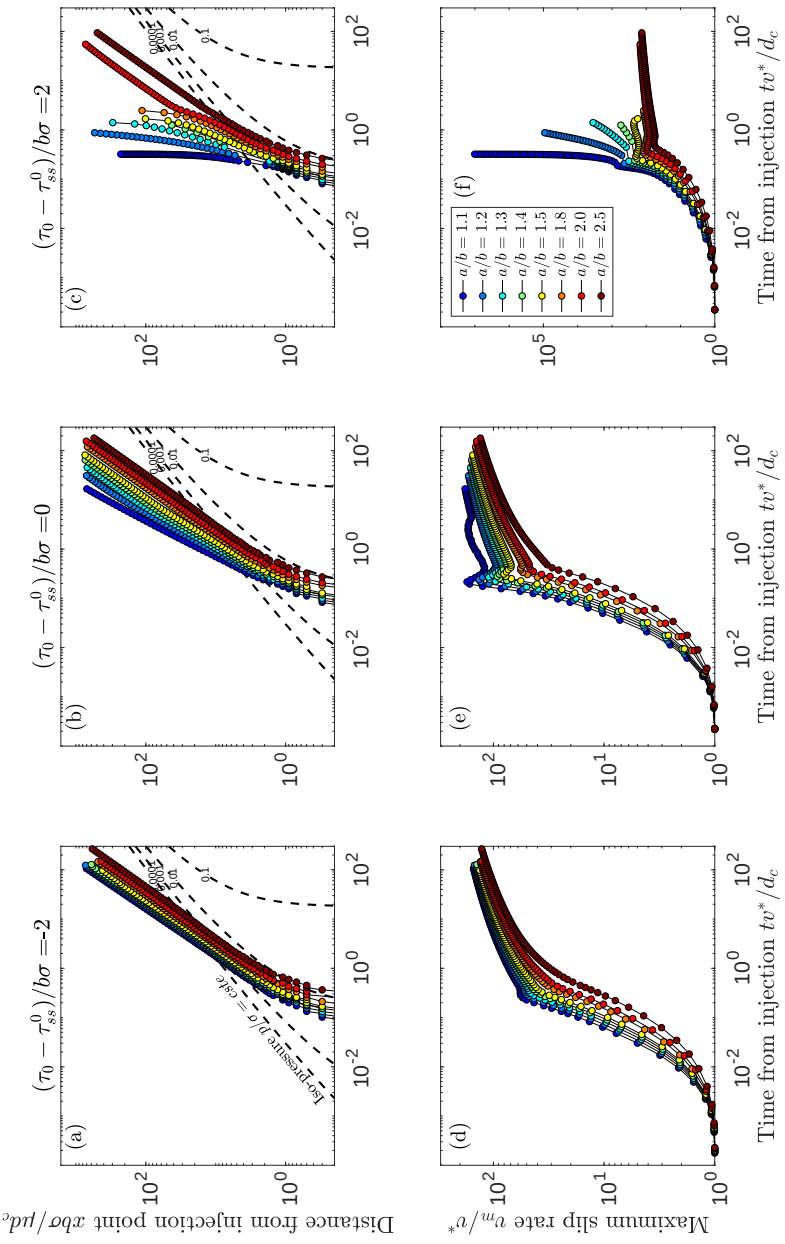

Figure 3: Shear crack half length (a,b,c) and maximum slip rate (d,e,f) as a function of time from the start of injection for all the fault scenarios investigated here. (a,d): Fault initially slightly below steady state ($\tau_0 - \tau_{ss}^0 = -2b\sigma$). (b,e): Fault initially at steady state ($\tau_0 - \tau_{ss}^0 = 0$). (c,f): Fault initially slightly above steady state ($\tau_0 - \tau_{ss}^0 = 2b\sigma$) . The color scale refers to the rate-and-state frictional parameter $\alpha = a/b$. Black dashed lines in figures (a,b,c) indicate iso-pressure levels. See figure 2 for details.

3.1. Phase I: initial slip rate acceleration

As shown in appendix Appendix A.1, the initial localized slip rate acceleration could be understood to the first order as a balance between the direct effect term $\alpha\dot{v}/v$ and the approximate rate of change of effective normal stress $f_0\dot{p}$ in the central region of the fault. The other terms appearing in the first equation of (9) being negligible. In this framework, the maximum slip rate v_m is reached where the pore pressure is maximum, that is at the injection point. It is shown in appendix Appendix A.1 that v_m evolves approximately as:

$$v_m(t) = exp(\sqrt{t/t_a}), \tag{12}$$

where t_a is a characteristic time scale given by:

$$t_a = \frac{\pi}{4}\frac{\alpha^2}{Df_0^2q^2}. \tag{13}$$

This first phase ends when steady state is reached at the fault center (see figure A.8), marking the onset of significant crack expansion. It is shown in appendix Appendix A.1, that the onset of phase II occurs at time t_I given by:

$$t_I \simeq t_a(\ln 2t_a)^2. \tag{14}$$

As illustrated in figure 4, equation (12) provides a good estimates of the exponential increase of the maximum slip rate on the fault. Furthermore, the expression (14) for t_I provides the correct order of magnitude for the transition time to phase II, in particular for small values of α. For larger values, it anticipates the transition by a factor of 2. This is certainly due to all the approximations leading to equation (14).

During phase I, we do not detect any significant increase of the length of the crack (no points for phase I in figures 3(a), (b) and (c)). This does not mean that the accelerating patch does not slightly expands: initially the slip rate is below the threshold used to track the crack size ($v = 10$). Because of the balance between the direct effect and the pore pressure rate, the size of the

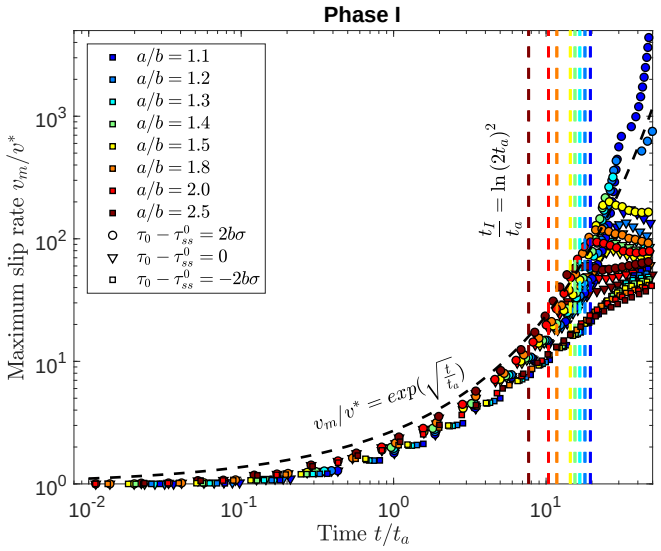

Figure 4: Normalized maximum slip rate increase during phase I. Colored symbols correspond to the different fault scenarios (different rate-and-state frictional parameter $\alpha = a/b$ and different initial stress). The black dashed line is the theoretical prediction of equation (12). The colored dashed lines are the theoretical estimates for the end of phase I (t_I) provided by equation (14).

accelerating patch is directly controlled by the diffusion length $\sqrt{Dt}$, as shown in figures A.9(a) and A.10(a).

3.2. Phase II: slip rate increase and crack expansion

The onset of phase II is characterized by a steepening of the slip rate profile at the crack tip (last blue profiles and first black profiles in figure 2(a) and (b)). Simultaneously, the position of the slip rate maximum v_m is shifted from the fault center to the crack front. The initiation of such a sharp slip front was observed for all the fault scenarios considered here. As noted earlier, the slip front then evolves in two different ways: either the peak slip rate increases, and the front accelerates in the case of an accelerating crack (figure 2(b-d)), or the peak slip rate decreases so that the sharp front dies away (figure 2(a-c)), leading to a smoother front propagating at a constant speed (steady crack). In this latter case, the slip rate is maximum at the crack center. In the following, we will make the distinction between the maximum slip rate v_m and the peak slip rate v_p, that is the slip rate at the tip of sharp propagating fronts. In the case of an accelerating crack (figure 2(b)), $v_m = v_p$.

3.2.1. Accelerating crack

In order to study in detail the dynamics of the accelerating crack, we concentrate on the fault scenarios characterized by $\alpha = 1.1$ or 1.2 and an initial state of stress above steady state ($\tau_0 - \tau_{ss}^0 > 0$), which provide the most characteristic examples of such a dynamics (figure 3). In appendix Appendix A.2.1, it is shown that the accelerating crack is characterized by a square-root shaped displacement profile at the crack tip, and a positive stress drop $\Delta\tau_{tip}$ near the tip of the crack (i.e. the difference between the initial stress and the residual stress left by the process zone at the crack tip). A quasi-static energy balance at the tip indicates that the crack half-length is approximately given by the characteristic length L_c defined by Rubin and Ampuero (2005):

$$L \sim L_c = \frac{1}{\pi}\left[\frac{\ln v_m\theta_0}{\ln\theta_0 - (\alpha-1)\ln v_m}\right]^2. \tag{15}$$

Furthermore, the crack expansion rate $\dot{L}$ is approximately given by the characteristic rupture speed v_c defined by Ampuero and Rubin (2008) as a function of the maximum (peak) slip rate v_m. From Ampuero and Rubin (2008), we thus have:

$$\dot{L} \sim v_c = 0.75 \frac{v_m}{\ln v_m \theta_0}. \tag{16}$$

As shown in figure 5(a) and (b), the results of the numerical simulations converge to the predictions of equations (15) and (16), for the two examples of accelerating cracks detailed here.

The simple quasi-static crack model defined by equations (15) and (16) provides an explanation to the observed diverging crack length and maximum (or peak) slip rate. Under velocity strengthening rheology ($\alpha > 1$) and an initial prestress above steady state ($\tau_0 - \tau_{ss}^0 = \ln \theta_0 > 0$), the two equations constrain L, $\dot{L}$, v_m (or v_p) and $\dot{v}_m$ to be increasing functions of time. In particular, according to (15), as v_m increases, L blows up and diverges at a finite slip rate v_l, approximately given by:

$$v_l = \theta_0^{1/(\alpha-1)}. \tag{17}$$

However, we did not try to find a closed form solution to equations (15) and (16) and we did not solve this system numerically. The solutions $L(t)$ and $v_m(t)$ would indeed be strongly influenced by our choice of initial conditions (poorly defined at the end of phase I), and by the fact that equation (15) is approached relatively slowly (see figure 5(a)). Note that in this case, since the pore pressure term does not enter into equation (15), the propagation is exclusively driven by the release of initial prestress. Beyond the limit speed v_l, the quasi-static crack model fails, since the stress drop at the crack tip (denominator in equation (15), see appendix Appendix A.2.1 for details) becomes negative.

More generally, such a mode of propagation is only possible if the stress drop at the crack tip is positive. In all the simulations this kind of crack front was observed, we computed the stress drop evolution $\Delta\tau_{tip}$. The results are reported

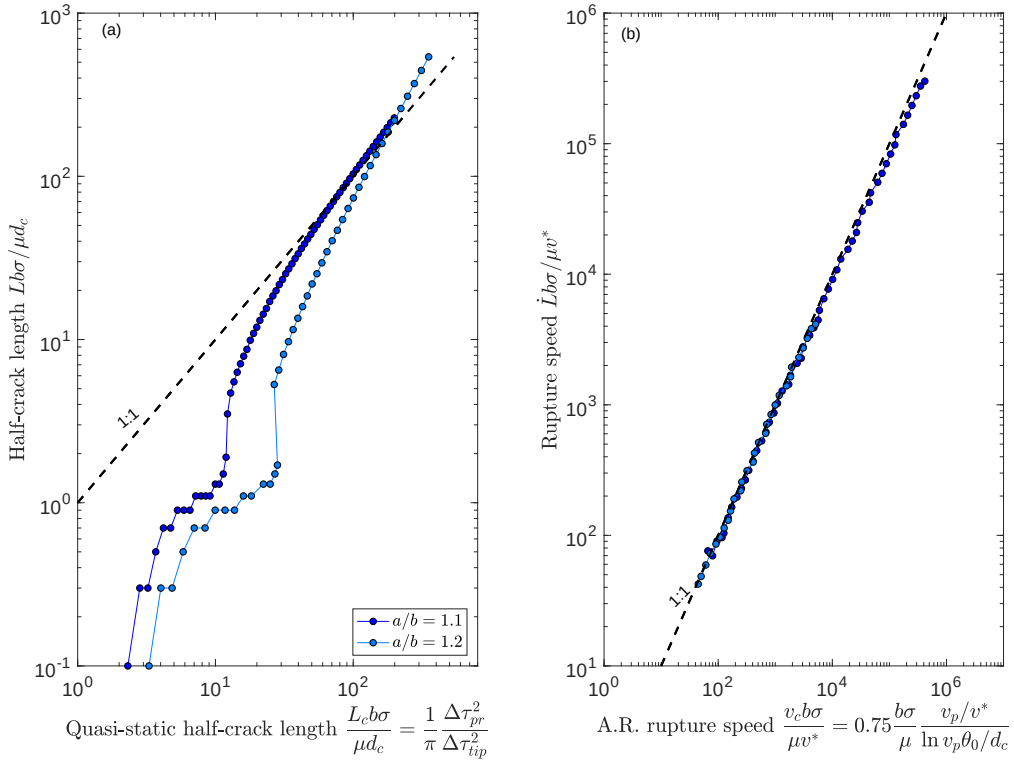

Figure 5: Numerical vs. theoretical dynamics of accelerating cracks, obtained with initial stress above steady state ($\tau_0 - \tau_{ss}0 = 2b\sigma$). (a): crack half-length as a function of the theoretical length L_c (expected from a quasi-static energy balance at the crack tip, equation (15)). $\Delta\tau_{pr}$ is the peak to residual stress drop, $\Delta\tau_{tip}$ is the stress drop at the crack tip (see main text for details). (b): rupture speed (crack expansion speed), as a function of the theoretical prediction by (Ampuero and Rubin, 2008) (A.R. rupture speed v_c, equation (16)). v_m is the maximum slip rate. Colored dots indicate the numerical solution. Black dashed lines indicate the perfect match between numerical solution and theoretical estimates L_c and v_c.

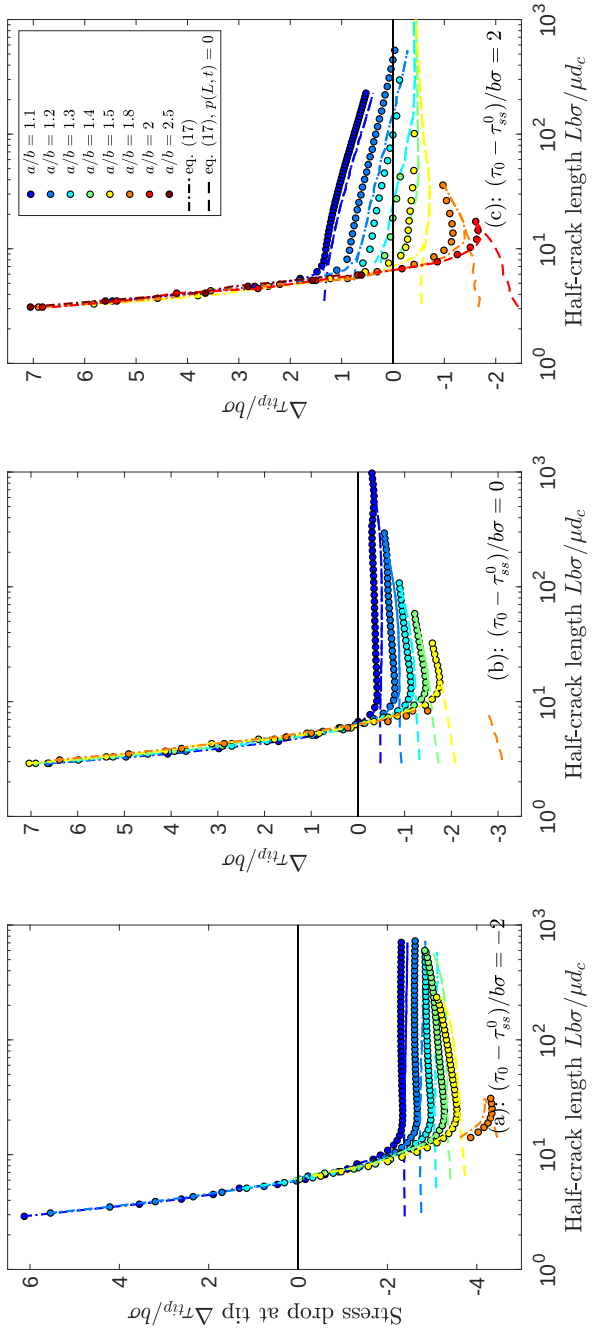

Figure 6: Stress drop at the crack tip $\Delta\tau_{tip}$ during crack expansion (phase II) for all the scenarios an accelerating crack was enough developped to be observed. (a): Fault initially slightly below steady state ($\tau_0 - \tau_{ss}^0 = -2b\sigma$). (b): Fault initially at steady state ($\tau_0 - \tau_{ss}^0 = 0$). (c): Fault initially slightly above steady state ($\tau_0 - \tau_{ss}^0 = 2b\sigma$). Color scale corresponds to the rate-and-state friction parameter $\alpha = a/b$. Dots are the numerical results. Dashed and dashed dotted lines are the approximations of equation (18). The balck horizontal line indicates $\Delta\tau_{tip} = 0$. The fault scenarios not represented (or partially represented) correspond to situations where the accelerating crack was too short lived.

in figure 6 as a function of the (increasing) crack length. $\Delta\tau_{tip}$ is always positive at the onset of the propagation, then it strongly decreases as crack propagation proceeds and eventually becomes negative. At larger crack length, $\Delta\tau_{tip}$ either increases smoothly if negative, or decreases smoothly if positive. As shown in figure 6, the evolution of $\Delta\tau_{tip}$ is well captured by the approximate expression of $\Delta\tau_{tip}$ provided in appendix Appendix A.2.1:

$$\Delta\tau_{tip}(t) = \ln\theta_0 - (\alpha - 1)\ln v_p(t) + f_0 p(L,t), \tag{18}$$

where $p(L,t)$ is the pressure at the crack front $x = L$ and time t. Initially, when the crack process zone is within the pressurized region, the third term dominates, so that $\Delta\tau_{tip}$ is positive. The initiation of an accelerating crack could therefore be attributed to the decrease of effective normal stress within the pressurized region. As the crack expands faster than the pressurized region, this term decreases, and the first two terms become important, until they dominate (figure 6). When the pore pressure term becomes negligible, the evolution of $\Delta\tau_{tip}$ becomes smoother.

The evolution of $\Delta\tau_{tip}$ shows that if in many cases, an accelerating crack could be initiated at early times, this kind of solution can not be sustained during the whole simulation, because $\Delta\tau_{tip}$ quickly becomes negative. This is typically what happens in figure 2(a,c). The only way of maintaining this accelerating crack beyond the pressurized zone is to keep the first two terms of equation (18) positive, that is if $v_p < v_l$. From equation (17), we see that if the initial stress is below steady state ($\theta_0 \leq 1$), then v_l is smaller than the initial slip rate $v = 1$, and the accelerating crack can not develop towards instability. For faults initially above steady state ($\theta_0 > 1$), we obtain $v_l = 4.85 \times 10^8$ for $\alpha = 1.1$, $v_l = 2.2 \times 10^4$ for $\alpha = 1.2$, which is near or above the observed maximum slip rates (figure 3(f)). Under stronger velocity strengthening properties ($\alpha > 1.2$), we get v_l between 3 and 800, which is of the order of (or below) the observed maximum slip rates. Equation (17) therefore provides a first order estimate of the range of slip rates that could be obtained on a prestressed velocity strengthening fault.

As the accelerating crack dies away, the simulations evolve towards a steady propagation, that is detailed in the next section.

3.2.2. Steady crack

It is shown in appendix Appendix A.2.2 that this second mode of crack propagation is to the first order controlled by a balance between the elasticity (i.e. the elastic stress transfers) and the approximate rate of effective normal stress change $f_0\dot{p}$. In other words, the crack evolves as if it were governed by a constant friction coefficient within the slipping zone. Here the pore pressure increase drives the crack expansion (and not the initial prestress). When assuming this simplified stress balance within the crack along with the conservation of total stress along the fault, it could be shown (appendix Appendix A.2.2) that the crack half size grows linearly in time as:

$$L(t) = v_r t = \frac{f_0 q D}{\lambda(\alpha - 1) - \ln \theta_0} t, \tag{19}$$

where v_r is a constant rupture speed. As during phase I, the maximum slip rate v_m is reached at the injection point, and approximately increases as the logarithm of time:

$$v_m(t) = c\left(1 + \ln\sqrt{\frac{t}{t_s}}\right), \qquad c = \frac{4 f_0 q D}{\pi}, \qquad t_s = 4\frac{\lambda^2(\alpha-1)^2 - \ln\theta_0{}^2}{f_0^2 q^2 D}. \tag{20}$$

c and t_s are a typical slip rate and a characteristic time scale respectively. In both equations (19) and (20), λ corresponds to the logarithm of maximum slip rate on the fault, which has been assumed constant in the derivations of appendix Appendix A.2.2. Since the maximum slip rate approximately increases logarithmically in time for the steady crack, the changes in $\lambda = \ln v_m$ are negligible compared to the linear increase of crack length L, and the variations of v_m. If we consider λ as the average value of $\ln v_m$ during phase II for the steady crack, we get numerically $4.6 < \lambda < 5.2$. In the following we therefore assume $\lambda = 5$.

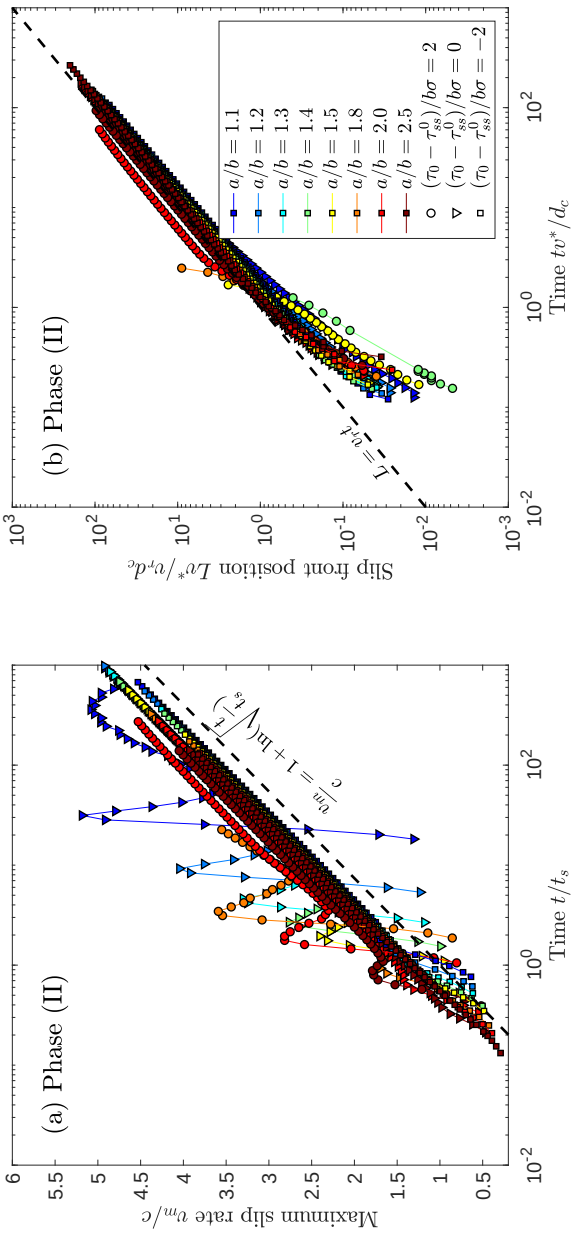

Figure 7: Normalized maximum slip rate (a) and normalized slip front position (b) for the simulations leading to a steady crack expansion during phase II. Only times $t > t_I$ are represented (phase II). Colored dots are the numerical results. The black dashed lines are the approximations of equations (19) and (20) the characteristic slip rate c, rupture speed v_r and time t_s are defined in the main text: equations (19) and (20).

Numerical simulations leading to a steady crack approximately converge to the predictions of equations (19) and (20), as illustrated in figure 7. For $t > 10t_s$, the maximum slip rate and the crack half size follow a logarithmic and linear increase respectively. The approach to the asymptotic solution for v_m is in some cases preceded by a quick oscillation, in particular for $\tau_0 - \tau_{ss}^0 = 2b\sigma$ and for small values of α. This corresponds to the transient phase (between phase I and II) where an accelerating crack is initiated, so that the maximum slip rate is the peak slip rate at the tip $v_m = v_p$. However, v_p quickly decreases as the accelerating crack can not propagate any further.

4. Discussion

We have shown that a fluid injection into a velocity strengthening rate-and-state fault initiates a slow (aseismic) slip event in the form of a shear crack expanding faster than pore pressure diffuses along the fault (the crack front neither follows an iso-pressure, nor expands diffusively as $\sqrt{t}$). Aseismic slip outpaces the pore pressure diffusion for the range of initial stress and frictional conditions analyzed here. This dynamics is similar to the results obtained by Cappa et al. (2018); Bhattacharya and Viesca (2019) in the case of significant permeability enhancement. We did not consider permeability enhancement, so that the strong slow slip response is essentially the result of the rate-and-state rheology.

We were able to highlight many new features about the dynamics of fluid driven slow slip under constant injection rate. Our results show two successive phases of evolution: in a first phase, slip abruptly accelerates around the injection point, and the crack remains within the pressurized zone. In a second phase, the crack expands along strike while the slip rate keeps increasing. Two modes of crack expansion were observed: an accelerated expansion characterized by diverging slip rate and rupture speed, or a steady crack expanding at a constant speed with a slip rate increasing as the logarithm of time. The accelerating crack could eventually lead to radiative slip rates (v_{sis} of the order

of 1cm.s^{-1}): assuming a reference slip rate $v^* = 10^{-9}$ m.s^{-1}, this would correspond in our simulations to a slip rate increase of 8 orders of magnitude. The accelerating crack could therefore be considered as the nucleation phase of a dynamic event, that would eventually stop when the slip rate reaches the limiting speed $v_l = \theta_0^{1/(\alpha-1)}$ defined in equation (17). The steady crack on the other hand only involves slow slip rates, so that it could be considered as ultimately stable. These two crack modes could be compared to the stability analysis by Garagash and Germanovich (2012); Azad et al. (2017), where a fluid driven aseismic crack either nucleates a dynamic instability if the initial stress τ_0 is larger than the residual stress τ_r of the slip-weakening friction law, or remains stable and aseismic if $\tau_0 < \tau_r$. Here we see that under rate-and-state friction, unstable cracks can develop up to seismic speeds if $v_l > v_{sis}$, which leads to (from the definition of v_l) :

$$f_0 + \ln \theta_0 > f_0 + (\alpha - 1) \ln v_{sis}, \tag{21}$$

which is nothing else than the initial stress τ_0 being larger than a residual (steady state) stress τ_r^a taken at the seismic slip rate v_{sis} according to the second equation of (10). Note that this result does not necessarily imply important initial stress that would be non-physical: as α goes to one, the initial deviation from f_0 leading to slip rate of seismic magnitude v_{sis} could be arbitrarely small. For $\alpha = 1.1$ and assuming $v_{sis} \simeq 10^9$, it is only necessary to perturb f_0 by 0.35 percent to promote dynamic failure. Considering typical values of friction parameters, along with a lithostatic normal stress at approximately 3 km depth, this implies an increase in shear stress of approximately 0.21 MPa from a reference value of 60 MPa. This order of magnitude is below the typical stress drop of earthquakes (Abercrombie, 1995; Allmann and Shearer, 2009). It is thus within the range of stress variations expected on tectonic faults. Under constant slip rate v_{sis}, rate-and-state friction indeed behaves as a slip weakening law, the steady state value of stress being the residual stress. This is typically what happens at the crack tip: slip rate instantaneously increases to v_{sis},

which remains approximately constant as the crack propagates further. The conditions leading to an unstable crack propagation are therefore equivalent to the conditions needed to nucleate a dynamic rupture under slip weakening law (Garagash and Germanovich, 2012; Azad et al., 2017).

An important difference between the rate-and-state response and the slip weakening response is the absence of a minimum stress (or pore pressure increase) to trigger a slip transient. This feature is similar to the spontaneous nucleation process on a velocity weakening rate-and-state fault (Rubin and Ampuero, 2005; Ampuero and Rubin, 2008).

We have shown that during phase I, the crack expansion occurs diffusively, following the pore pressure diffusion. A spontaneous expansion starts at the begining of phase II. We defined the characteristic time t_I for the transition to phase II that could also be used to define a characteristic crack length L_I at the transition to phase II. Since the initial crack expansion is diffusive, we have $L_I \simeq \sqrt{Dt_I}$. t_I and L_I are the time needed to start crack expansion, and the critical length allowing crack expansion. If an accelerating crack develops, t_I and L_I could therefore be used as estimates for the time to instability and the critical crack length for instability. Assuming that variations in $\ln t_a$ are negligible compared to changes in t_a, we can assume from equation (14) that $t_I \propto t_a$, and from the definition of t_a (13) we get:

$$\begin{cases} t_I \propto \dfrac{\alpha^2}{D f_0^2 q^2} \\ L_I \propto \dfrac{\alpha}{f_0 q}. \end{cases} \tag{22}$$

This simple scaling indicates first that the injection scenario controls the transition to instability: t_I and L_I decrease as the injection rate increases. A decrease of time to instability with increasing injection rate was already obtained by Garagash and Germanovich (2012); Azad et al. (2017), in the framework of slip-weakening friction. However, the authors did not observe a significant change in the critical length with the injection scenario. Under rate-and-state friction, the critical length and time to instability also depend on the parameter α: stronger

strengthening behavior (large α) leads to a delayed t_I and a larger L_I.

Note that for the range of initial stress investigated (in the vicinity of steady state at the reference speed), the dynamics of phase I does not significantly depend on the initial state of stress, as observed by Garagash and Germanovich (2012); Azad et al. (2017). As shown in appendix A, phase I is essentially controlled by a balance between the direct effect of the friction law and the rate of pore pressure change, so that only the initial slip rate matters and the state evolution could be neglected. Since we have considered situations where initial stress is controlled by the initial value of the state variable, the initial stress has no real influence on the dynamics of phase I. Considering a much higher or smaller value of the initial state variable may break the balance between the direct effect and the pore pressure change, so that the initial stress would influence the dynamics of phase I (in particular t_I and L_I). Alternatively, considering a higher initial stress by imposing a higher initial slip rate would make the dynamics of phase I more sensitive to the initial stress (in particular t_I and L_I). Therefore, we do not rule out the possibility that initial stress influences the transition to the (eventually accelerated) crack expansion.

Here we have decided not to investigate extreme values of the initial state variable in order to remain under initial stress conditions close to steady-state friction. Such close to steady state conditions are expected to prevail on aseismic faults that have not experienced significant stress perturbations for a long time (at least longer than the characteristic time for slip relaxation, that could be estimated from the observed duration of afterslip following large earthquakes, or from the characteristic duration of aftershock sequences driven by frictional afterslip. This characteristic time is of the order of hours to years (Helmstetter and Shaw, 2009; Schaff et al., 1998)). Even following a stress perturbation, a velocity strengthening fault remains close to steady-state (Perfettini and Ampuero, 2008; Dublanchet et al., 2013). We therefore expect the probability of a fault to be far from steady-state to be very small. The simulations performed from initial steady-state conditions and the steady-crack solution are therefore the most relevant results of this study concerning the understanding of tectonic

fault behavior.

The crack expansion characterizing the second phase occurs either at an increasing rupture speed (accelerating crack) or at a constant rupture speed (steady crack). The accelerating crack being a transient state (until a limit speed is reached), we expect it to evolve towards a dynamic rupture, or to the steady crack (as observed for faults initially above steady state and characterized by intermediate frictional parameter α) . A dynamic rupture is controlled by inertia, so that rupture speed is a fraction of the shear wave speed of the elastic medium. If slowing down to the steady crack, the expansion will ultimately proceed at constant rupture speed v_r provided by equation (19). As shown in appendix Appendix A.2.2, the constant rupture speed is a consequence of the linear increase of average pore pressure under constant injection rate. Considering a different injection scenario could lead to a different dynamics of crack expansion. Many seismological observations show a migration of micro-earthquakes and tremor activity along faults at a constant speed (Duverger et al., 2015; Roland and McGuire, 2009; Ghosh et al., 2010; Houston et al., 2011) along with clear evidences that such activity is triggered by a slow aseismic slip event. The constant migration speed of seismic activity could therefore be related to an aseismic slip event propagating at a constant speed. Our result suggest that such phenomena are compatible with a triggering mechanism involving a fluid over-pressure emanating from a local and constant injection rate.

We show in appendix Appendix A.2.2 that the steady crack rupture speed v_r results from a stress balance at the scale of the entire fault. The reduction of frictional stress (related to the effective normal stress decrease) is balanced by the velocity strengthening rheology (shear stress increase caused by slip rate acceleration) on the cracked region. The reduction of effective stress is essentially accommodated by an expansion of the high slip rate region, rather by a stronger increase of slip rate. Assuming that the parameter λ in equation (19)

is a measure of the log of the maximum slip rate, v_r could be rewritten as:

$$v_r = \frac{f_0 q D}{\tau_r^s - \tau_0}, \tag{23}$$

where $\tau_r^s = f_0 + (\alpha - 1)\lambda$ could be understood as a typical (steady-state) residual stress within the crack from equation (10), that is larger than the initial stress τ_0 for the steady propagating crack. Here again, the dynamics of the steady crack strongly depends on the difference between the initial stress and a residual stress of the friction law. v_r is expected to diverge as the initial stress gets closer to τ_r^s. If $\tau_0 > \tau_r^s$ we enter the accelerated crack solution. The importance of $\tau_0 - \tau_r^s$ in the steady crack dynamics is here again analog to the slip weakening case (Garagash and Germanovich, 2012; Azad et al., 2017). Hydraulic properties also contribute to the crack expansion speed: a higher injection rate or a stronger diffusivity leads to an increase of v_r.

An important result to note is that both τ_r^a controlling the possibility of dynamic slip rates, and τ_r^s allowing the steady crack propagation correspond to a residual steady-state stress within the expanding crack at zero pore pressure, whatever crack regime prevails. τ_r^s and τ_r^a could therefore be unified so that the relevant parameter incorporating the effect of prestress conditions and the parameter α is the (slip-rate dependent) residual stress within the crack τ_r at zero pore pressure. The different crack propagation regimes are therefore controlled by $\tau_0 - \tau_r$.

So far we have only considered a single injection scenario consisting in a constant injection rate (or fixed pore pressure gradient at the origin). Other injection scenarios could be investigated, in particular involving a finite duration of injection. When the injection stops, pore pressure progressively decreases along the fault, and as the pore pressure rate becomes negligible, the fault is essentially controlled by a balance between elasticity and friction. At large time after injection (over timescales exceeding the diffusion timescale L_0^2/D on the entire fault) the system behaves as a velocity strengthening fault responding to an instantaneous stress perturbation. This problem has already been studied by

Perfettini and Ampuero (2008), showing that the maximum slip rate ultimately relaxes back to the steady state reference velocity v^* following a $1/t$ decay. However, the behavior at intermediate times needs to be further investigated. Different scenarios could also be analyzed, involving a controlled overpressure at the injection point (Garagash and Germanovich, 2012), or a propagating hydraulic fracture (Azad et al., 2017). Slip and stress induced permeability enhancement seems also to play an important role in fluid induced aseismic slip as shown by the in-situ hydro-shearing experiments (Guglielmi et al., 2015; Cappa et al., 2018; Bhattacharya and Viesca, 2019). If permeability enhancement increases the aseismic slip response under slip-weakening friction, more efforts need to be done to evaluate this effect under rate-and-state conditions.

Finally, we did not investigate here the whole rate-and-state spectrum: we did not consider other state evolution laws, such as the slip law (Ruina, 1983). We do not present any results about the velocity weakening behavior. Nevertheless, our results suggest that in the absence of strengthening, the accelerated crack would be favored by velocity weakening rheology, leading to dynamic ruptures if the fault is large enough for the nucleation to fully develop. If nucleation on dry, velocity weakening, rate-and-state faults has been largely explored (Rubin and Ampuero, 2005; Ampuero and Rubin, 2008; Dublanchet, 2017), fluid induced earthquake nucleation needs to be further investigated.

5. Conclusion

The effect of a local injection of fluid into a stable velocity weakening fault could be summarized as follows: in a first step, the reduction in effective normal stress triggers a slip acceleration in the form of a shear crack confined to the pressurized zone. During this first phase, slip rate increases exponentially in time, and the crack expands diffusively along strike. In a second phase, the shear crack expands much faster than the pore pressure diffuses, and the regime of slip rate increase changes. The transition to the expansion phase is facilitated by a larger injection rate, and frictional properties closer to the

weakening transition $a/b = 1$. During phase II, we observe either an accelerating crack regime, where slip rate and rupture speed blow up in a finite time, or a steady crack expansion characterized by a constant expansion speed and a logarithmic increase of maximum slip rate. The transition between the two regimes could be understood in terms of the difference between the initial stress along the fault τ_0, and the residual stress left within the crack τ_r. The accelerating crack regime is obtained when $\tau_0 > \tau_r$, while the steady crack occurs if $\tau_0 < \tau_r$. The rupture speed of the steady crack decreases approximately as the inverse of $\tau_r - \tau_0$, and increases linearly with the injection rate. Considering the possible stress conditions on tectonic faults, the steady crack is the most probable reactivation scenario expected from these results. The slip response of a rate-and-state fault to a fluid injection is therefore controlled by the frictional properties, the injection history, and the initial stress conditions. The numerical and theoretical results presented here provide some new insights about the hazards associated with fluid operations at depth, by demonstrating quantitative relationships between injection parameters and fault slip response.

Appendix A.

In this section, we derive approximate expressions for the slip-rate profiles, the maximum slip rate $v_m(t)$ and the half-crack size evolution $L(t)$. As mentioned in the main text, the slip rate evolution during a fluid injection could be decomposed into two phases: in the early phase (phase I), slip rate increases exponentially on a small patch centered on the injection point. In the second phase, the slip rate increases further while the accelerating crack expands along strike. Recall that in all the following developments we make use of the non-dimensional notations defined in the second section.

Appendix A.1. Early slip acceleration

As shown in figure A.8(a,d,g), the early phase is characterized to the first order by a balance between the shear stress rate related to the pore pressure

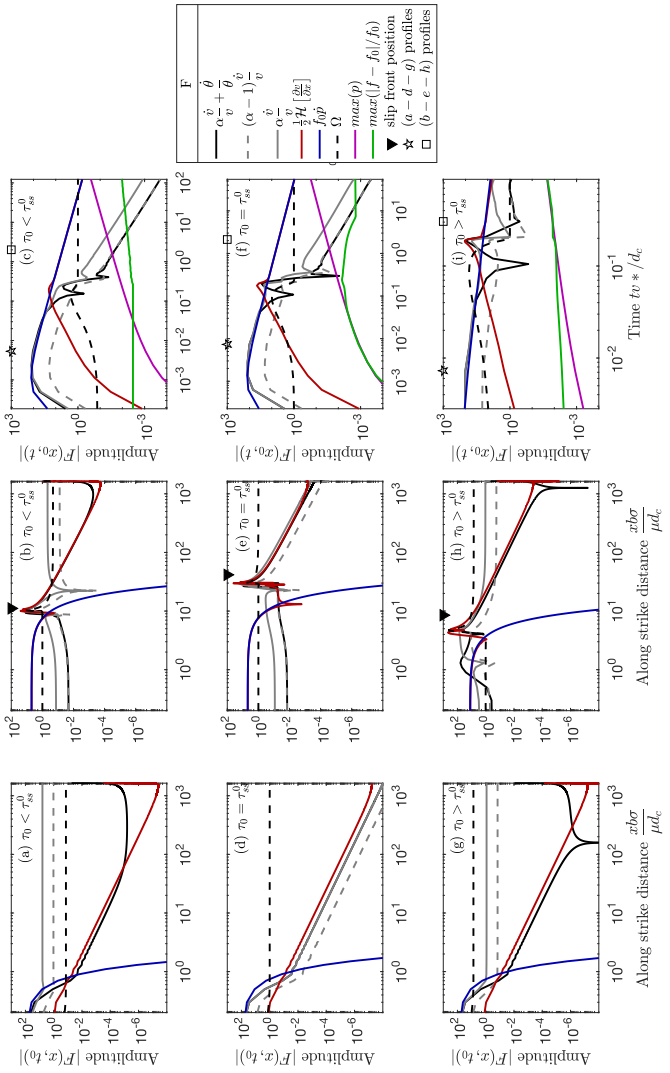

Figure A.8: Stressing rate contributions along the fault, for the fault scenarios with $\alpha = a/b = 1.2$. The different lines represent the different terms of the stressing rate balance (9), along with the distance to steady state $\Omega = v\theta$ (dashed black line), the maximum value of pore pressure p (purple solid line), and the deviation of the friction coefficient f from its reference value f_0 (green line). The two left columns represent the different contributions along strike (only the right half fault is represented) at two selected instants ($t = t_0$): one during phase I (left column), the second during phase II (middle column). The black triangle marks the position of the crack front. The right column represents the different contributions at the fault center ($x = x_0$) as a function of time from the start of injection. The black star and the black square indicate the time corresponding to the profiles of the left column and the middle column respectively. (a,b,c): Fault initially slightly below steady state ($\tau_0 - \tau_{ss}^0 = -2b\sigma$). (d,e,f): Fault initially at steady state ($\tau_0 - \tau_{ss}^0 = 0$). (g,h,i): Fault initially slightly above steady state ($\tau_0 - \tau_{ss}^0 = 2b\sigma$). Note that non-dimensional notation is used in the legend.

rate ($f\dot{p}$) and the changes in friction coefficient ($\alpha\dot{v}/v + \dot{\theta}/\theta$), in the central region of the fault where slip accelerates ($|x| < 1$ in figures A.8(a,d,g)). The elastic stress transfers (Hilbert transform term in the first equation of (9)) are negligible. Outside this central region, the elastic stress transfers dominate over the pore pressure variations. Note also that in figures A.8(a,d,g), the black solid curve overlaps the gray solid line within the pressurized zone, so that the state evolution term is negligible and the changes in the friction coefficient are dominated by the direct effect $\alpha\dot{v}/v$. This balance is maintained in particular at the crack center during the whole duration of phase I (see figures A.8(c,f,i)). Furthermore, during this early phase, $f \simeq f_0$ and $p << 1$ (figure A.8(c,f,i)) so that around the injection point, the system (9) approximately reduces to:

$$\alpha\frac{\dot{v}}{v} = f_0\dot{p}, \tag{A.1}$$

which leads to, after integrating from $t = 0$ to t along with $v(x, 0) = v_0 = 1$ and $p(x, 0) = 0$:

$$v = e^{f_0 p/\alpha}. \tag{A.2}$$

The maximum slip rate v_m is thus expected to occur at the injection point $x = 0$, where the fluid pressure is maximum. Making use of equation (6) at $x = 0$, we get:

$$v_m(t) = e^{\sqrt{t/t_a}}, \qquad t_a = \frac{\pi}{4}\frac{\alpha^2}{Df_0^2q^2}. \tag{A.3}$$

The state evolution term could also be considered in these developments, in particular if the distance to steady state $\Omega = v\theta$ is significant. If $\Omega << 1$ for instance, we have from the state evolution law (3) $\theta \simeq \theta_0 + t$ (Helmstetter and Shaw, 2009), leading to a slip rate of the form:

$$v = \frac{e^{f_0 p/\alpha}}{(\theta_0 + t)^{1/\alpha}}. \tag{A.4}$$

Alternatively, if $\Omega >> 1$, the state evolution law leads to $\dot{\theta}/\theta \simeq -v$ (Helmstetter and Shaw, 2009), so that the stress balance could be integrated as:

$$v = \frac{e^{f_0 p/\alpha}}{1 - \Pi(t)/\alpha}, \tag{A.5}$$

where $\Pi(t)$ is given by:

$$\Pi(t) = \int_0^t e^{f_0 p(t')/\alpha} dt'. \tag{A.6}$$

It can be seen in figure A.9(a) and A.10(a), that approximations (A.4) and (A.2) are supported by our numerical solutions during the initial phase of slip rate evolution, for the two cases $\tau_0 - \tau_{ss}^0 = -2b\sigma$ and $\tau_0 - \tau_{ss}^0 = 0$ respectively, even at large distances from the pressurized zone. The maximum slip rate at the fault center v_m (figures A.9(d), A.10(d) and 4) is in any case close to the simple expression (A.3). Note that the grid used to compute the numerical solution does not allow to get the slip rate exactly at $x = 0$, and the maximum slip rate obtained numerically is instead the slip rate at $x = \pm h/2$, h being the grid size, which underestimates the maximum slip rate. The agreement between numerical and analytical solution is improved when using expression (A.2), with the pressure computed at $x = \pm h/2$.

As illustrated in figures A.8(c), (f) and (i), this balance between the direct effect and the pore pressure rate remains valid until the injection region reaches steady state. This could be seen with the evolution of the distance to steady-state $\Omega = v\theta$ at the injection point (recall that $\Omega = 1$ corresponds to steady state). Afterwards, the elastic interaction term $\mathcal{H}[v']$ becomes dominant over the pore pressure rate term, and equilibrates the friction coefficient variations $(\alpha\dot{v}/v + \dot{\theta}/\theta)$ at the crack center. In order to get an approximate duration for phase I, we need an expression for the evolution of Ω at the fault center. From the definition of Ω, and the state evolution law (3), we have:

$$\frac{\dot{\Omega}}{\Omega} = \frac{\dot{v}}{v} + \frac{\dot{\theta}}{\theta} = \frac{\dot{v}}{v} + v\left(\frac{1}{\Omega} - 1\right). \tag{A.7}$$

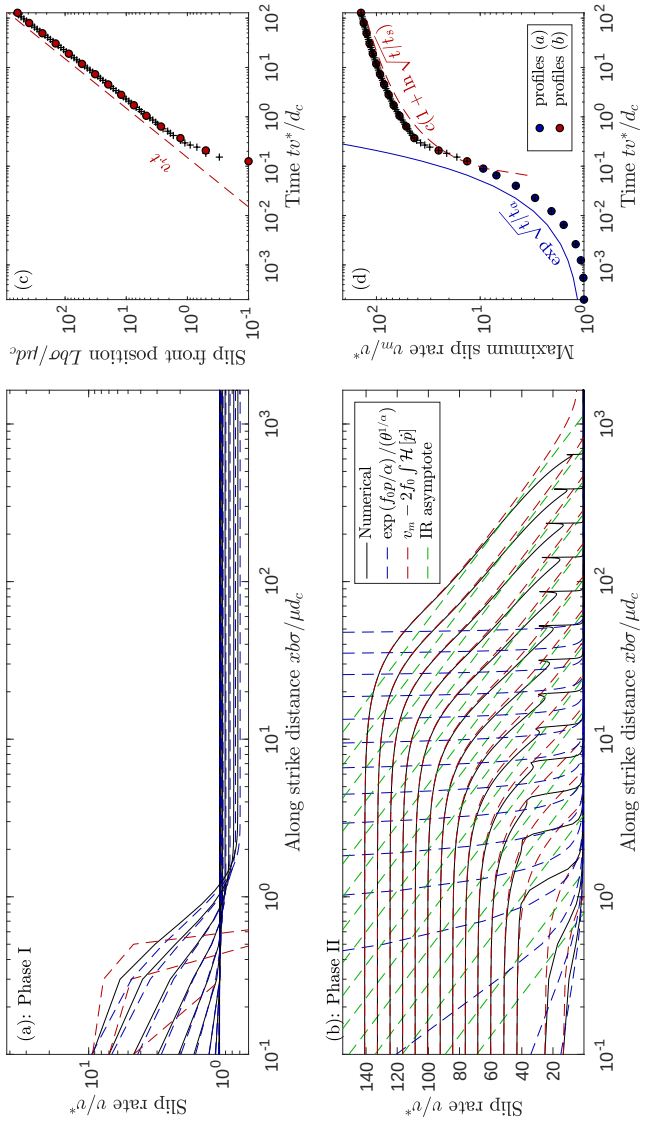

Figure A.9: Detail of slip rate evolution on a fault initially below steady state ($\tau_0 - \tau_{ss}^0 = -2b\sigma$) and characterized by a rate-and-state parameter $\alpha = a/b = 1.4$, evolving towards the steady crack solution. (a): Slip rate profiles during phase I. (b): Slip rate profiles during phase II. Here again in (a,b) only the right half fault is represented (the solution is symmetric). Black profiles correspond to the numerical solution, and the colored ones to the different possible approximations mentioned in the legend. Here again, non dimensional notations are used in the legend. The blue dashed profiles correspond to the approximation (A.4) expected during phase I. The red dashed profiles correspond to the approximation (A.23) suggested for phase II. The green dashed line is the simplified form of equation (A.23) in the intermediate distance range (IR): equation (A.26). (c): Crack half-length evolution. (d): Maximum slip rate evolution. The blue dots in (d) indicate the time and the maximum slip rate of each profile of (a). The red dots in (c) and (d) correspond to the profiles shown in (b). The blue solid line in (d) is the approximation (A.3) for the evolution of maximum slip rate during phase I. The red dashed lines in (c) and (d) indicate the approximations (A.36) and (A.37) for the crack half-length and the maximum slip rate during phase II.

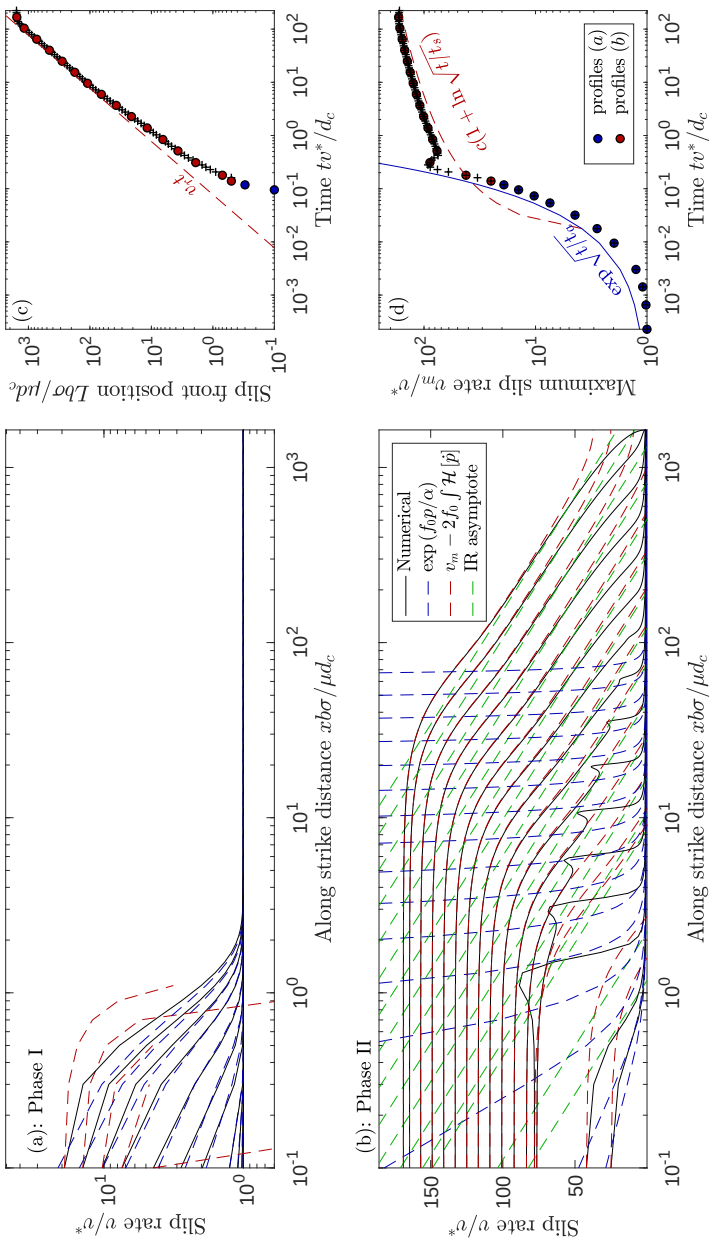

Figure A.10: Same as figure A.9 for a fault initially at steady state ($\tau_0 - \tau_{ss}^0 = 0$) and characterized by a rate-and-state parameter $\alpha = a/b = 1.4$, evolving towards the steady crack solution. Note that the blue dashed profiles correspond here to the approximation (A.2).

As shown in figures A.8(f) and (i), if the fault is initially above steady state $\Omega \geq 1$, phase I is characterized by $\Omega > 1$. We thus assume $\Omega >> 1$, so that equation (A.7) becomes:

$$\frac{\dot{\Omega}}{\Omega} = \frac{\dot{v}}{v} - v. \tag{A.8}$$

At the injection point ($x = 0$), this equation could be integrated for Ω making use of the approximate expression (A.3), leading to:

$$\ln \frac{\Omega}{\Omega_0} = \sqrt{\frac{t}{t_a}} - 2t_a \left[e^{\sqrt{t/t_a}} \left(\sqrt{\frac{t}{t_a}} - 1 \right) + 1 \right], \tag{A.9}$$

where Ω_0 is the initial value of Ω. This expression leads to first an increase followed by a decrease of Ω as the slip rate blows up. The end of phase I occurs when $\Omega = 1$. In our simulations, this occurs at a time $t_I >> t_a$, satisfying the last expression for $\Omega = 1$. For a $|\ln \Omega_0| << \sqrt{t_I/t_a}$, as this is approximately the case in our simulations, we end up with the following approximate expression for t_I:

$$t_I = t_a \left(\ln 2t_a \right)^2. \tag{A.10}$$

If the fault is initially slightly below steady-state, Ω increases during phase I, an quickly gets higher than 1 (figure A.8(c)). We will therefore use the same expression of t_I for all the initial stress conditions assumed here.

Appendix A.2. Slip acceleration and crack expansion

During the second phase (i.e. for $t > t_I$), slip on the fault consists in an expanding and accelerating crack of half size $L(t)$. As shown in figures 2 and 3, two modes of crack expansion are observed: an accelerated crack propagation, where maximum slip rate and crack size blow up in a finite time, or a steady crack propagation, where expansion occurs at a constant rate, and slip rate increases smoothly. The accelerated crack propagation dominates at early times, but most of the simulations performed here ultimately lead to a steady crack expansion.

Appendix A.2.1. Accelerated expansion

Here we study the accelerating crack dynamics. For that we focus on the fault scenario $\tau_0 - \tau_{ss}^0 = 2$, $\alpha = 1.1$. The change of slip rate v, slip δ and stress in the vicinity of the crack tip during the propagation are illustrated in figure A.11. Following the analysis by (Ampuero and Rubin, 2008; Rubin and Ampuero, 2009) for the nucleation pulses under velocity weakening conditions, the shape of the slip profiles (figure A.11) suggest a scaling of the form:

$$\delta(x,t) = \psi_0(t) f(X) \simeq 1.5\psi_0(t)\sqrt{X}, \tag{A.11}$$

where $\psi_0(t) = \ln v_m \theta_0$ is a scaling factor introduced by Rubin and Ampuero (2005); Ampuero and Rubin (2008); Rubin and Ampuero (2009), and $X = x - L(t)$ is the distance to the crack tip.

The stress profiles show a progressive increase of stress from the initial stress (at large X) to the peak stress at the crack tip ($X = 0$), then a weakening over a process zone of size W until reaching a constant value of residual stress within the crack. The residual stress is the steady state frictional stress approximately at the maximum slip rate v_m. As shown by Rubin and Ampuero (2005) and in figure A.11(c), the process zone width under rate-and-state friction is of the order of $W = 1$ when considering the ageing law. Note also that the stress outside the crack approximately decreases as the inverse of the square root distance from the tip (as expected when taking the Hilbert transform of the slip gradient, assuming the simple form (A.11)).

At the crack tip, the energy release rate G balances the fracture energy G_c. From (Rubin and Ampuero, 2005), the (non-dimensional) fracture energy for such a crack is given by:

$$G_c = \Delta\tau_{pr}^2, \tag{A.12}$$

where $\Delta\tau_{pr}$ is the difference between the peak τ_p and the residual stress τ_r at the tip. The (non-dimensional) energy release rate is approximately given by

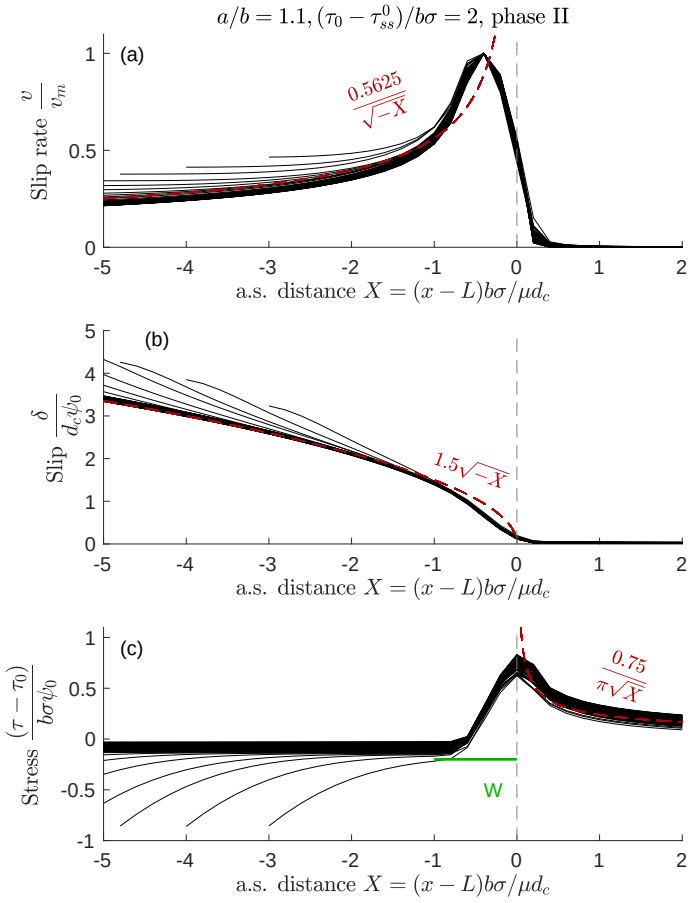

Figure A.11: Details of the slip rate (a), slip (b) and stress (c) changes in the vicinity of an accelerating crack tip, obtained on fault initially above steady state ($\tau_0 - \tau_{ss}^0 > 0$) and characterized by a rate-and-state friction parameter $\alpha = 1.1$. X is the distance to the crack tip: x being the along strike distance and L the half length of the crack. Slip and stress profiles are normalized by $\psi_0 = \ln(v_m\theta_0/d_c)$, v_m being the maximum (peak) slip rate. Black lines are the numerical solution, red dashed lines are the approximate profiles. See main text for details. The dashed vertical gray line indicates the crack tip (defined here as the position of the peak stress).

(Freund, 1998):

$$G = \pi \Delta \tau_{tip}^2 L, \tag{A.13}$$

where $\Delta\tau_{tip}$ is the difference between the initial stress τ_0 and the residual stress τ_r left by the process zone. Following the developments of Rubin and Ampuero (2005) for this kind of crack front, we have:

$$\begin{cases} \tau_0 = f_0 + \ln \theta_0 \\ \tau_p \simeq (f_0 + \alpha \ln v_m + \ln \theta_0)\,[1 - p(L,t)] \\ \tau_r \simeq [f_0 + (\alpha - 1) \ln v_m]\,[1 - p(L,t)]\,. \end{cases} \tag{A.14}$$

We end up with:

$$\begin{cases} \Delta\tau_{pr} = \tau_p - \tau_r \simeq \ln v_m \theta_0\,[1 - p(L,t)] \\ \Delta\tau_{tip} = \tau_0 - \tau_r \simeq \ln \theta_0 - (\alpha - 1) \ln v_m + f_0 p(L,t), \end{cases} \tag{A.15}$$

When the accelerating crack is well developed, the crack tip is far from the pressurized zone, so that $p(L,t) << 1$ and can be neglected in the above expressions. The expression for $\Delta\tau_{tip}$ has therefore been simplified assuming that p and the slip dependent component of the friction coefficient are small deviations from the reference normal stress 1 and the reference friction coefficient f_0 respectively. We have therefore neglected terms of second order. The last term in this expression quickly becomes also negligible as the crack expansion proceeds (see figure 6).

Neglecting the pressure at the crack tip, the energy balance ($G = G_c$) leads, after making use of expressions (A.15), to the following expression for the crack half length L:

$$L = \frac{1}{\pi} \left[\frac{\ln v_m \theta_0}{\ln \theta_0 - (\alpha - 1) \ln v_m} \right]^2. \tag{A.16}$$

Another feature of such a propagating crack shown by (Ampuero and Rubin, 2008) is that the rupture speed (or expansion speed $\dot{L}$) is controlled by the maximum slip rate v_m. Following (Ampuero and Rubin, 2008), we should ap-

proximately have:

$$\dot{L} = 0.75 \frac{v_m}{\ln v_m \theta_0}. \tag{A.17}$$

The two equations (A.16) and (A.17) govern the coupled evolution of v_m and L during the crack expansion.

Note that the form (A.11) leads to a slip rate v that follows:

$$v = \dot{\psi}_0 f(X) - \psi_0 \dot{L} f'(X). \tag{A.18}$$

If we neglect the first term, we get, after making use of expression (A.17):

$$v \simeq -0.75 v_m f'(X) \simeq 0.5625 \frac{v_m}{\sqrt{X}}, \tag{A.19}$$

which provides a good approximation to the simulated slip-rate profiles within the crack (see figure A.11(a)).

Appendix A.2.2. Steady expansion

Here we concentrate on the steady expansion phase, typically illustrated in figures 2(a,c), A.9(b) and A.10(b). Within the crack ($x < L(t)$), frictional changes become negligible compared to the elastic stressing rate and the stressing related to the pore pressure changes, as shown in figure A.8(b,c,e,f). Note that during this phase the inner part of the crack has evolved to the frictional steady state. The slip evolution is therefore controlled to the first order by a balance between the two terms on the right-hand side of the first equation of (9). Since during this phase as well $f \simeq f_0$ (figure A.8(c,f)), the slip rate evolution within the crack is approximately given by :

$$\frac{1}{2} \mathcal{H}\left[v'\right] = f_0 \dot{p}. \tag{A.20}$$

This last equation could be inverted, and making use of the inverse property of the Hilbert transform ($\mathcal{H}\left[\mathcal{H}\left(f\right)\right] = -f$ for any functional f (King, 2009)), we

get:

$$v' = -2f_0\mathcal{H}\left[\dot{p}\right] = -2f_0 q\sqrt{\frac{D}{\pi t}}\mathcal{H}\left[e^{-\eta^2}\right] = -\frac{4f_0 q}{\pi}\sqrt{\frac{D}{t}}D_w(\eta), \tag{A.21}$$

where D_w is the Dawson's function (Temme, 2010) defined as:

$$D_w(\eta) = e^{-\eta^2}\int_0^\eta e^{y^2}dy. \tag{A.22}$$

In writing equation (A.21) we have used the time derivative of the pore pressure field (6), the Hilbert transform of a Gaussian function and the scaling property of the Hilbert transform (King, 2009). Equation (A.21) could be further integrated with respect to x leading to:

$$v(x,t) = v_m(t) - \frac{8f_0 qD}{\pi}\int_0^\eta D_w(\xi)d\xi, \tag{A.23}$$

where $v_m(t) = v(0,t)$. Equation (A.23) could be further simplified, considering the asymptotic expansion of D_w at small and large η. We have :

$$\begin{cases} D_w(\eta) = \eta + o(\eta^3), & \text{as } |\eta| \to 0 \\ D_w(\eta) = \dfrac{1}{2\eta} + o(\dfrac{1}{\eta^3}), & \text{as } |\eta| \to +\infty. \end{cases} \tag{A.24}$$

In the following we will therefore make the assumption that:

$$\int_0^\eta D_w(\xi)d\xi \simeq \begin{cases} \int_0^\eta \xi d\xi = \dfrac{\eta^2}{2}, & \text{if } \eta < 1 \\ \int_0^1 \xi d\xi + \int_1^\eta \dfrac{d\xi}{2\xi} = \dfrac{1}{2}\left(1 + \ln\eta\right) & \text{if } \eta > 1 \end{cases} \tag{A.25}$$

The slip rate inside the crack (A.23) could therefore be approximated as:

$$v(x,t) \simeq v_m(t) - \begin{cases} \dfrac{4f_0 qD}{\pi}\eta^2, & \text{if } \eta < 1 \\ \dfrac{4f_0 qD}{\pi}\left(1 + \ln\eta\right) & \text{if } \eta > 1 \end{cases} \tag{A.26}$$

As shown in figures A.9(b) and A.10(b), the expression (A.23) provides a good approximation to the slip rate within the crack. These figures also show that the second expression of (A.26), labeled IR in the figures, could be used as an

approximation for the slip rate profiles at intermediate distances between the crack center and the crack tips. Note that the intermediate asymptote (IR, second expression in (A.26)) goes to minus infinity as x goes to infinity, at a given fixed time. This expression is therefore no longer valid at least when it vanishes. The zero of this expression could be used as an approximation of the crack tip position $L(t)$ as illustrated in figures A.9(b) and A.10(b). We therefore have the following relationship between $v_m(t)$ and $L(t)$:

$$v_m(t) \simeq \frac{4 f_0 q D}{\pi} \left(1 + \ln \frac{L(t)}{2\sqrt{Dt}}\right). \tag{A.27}$$

At this point we have one equation relating two unknowns: the crack tip (or slip front) position $L(t)$, and the maximum slip rate $v_m(t)$. A second expression could be obtained by considering the quasi-static shear stress balance on the entire fault. The global shear stress balance reads:

$$\int_{-\infty}^{+\infty} \left[\tau(x,t) - \tau_{el}(x,t)\right] dx = 0, \tag{A.28}$$

which leads to (from equations (1) and (5)):

$$\int_{-\infty}^{+\infty} \left[(f_0 + \alpha \ln v + \ln \theta)(1-p) - \tau_0 + \frac{1}{2}\mathcal{H}\left[\delta'\right]\right] dx = 0, \tag{A.29}$$

Since we consider here an initial slip rate uniform on the fault $v = 1$ along with a uniform $\theta = \theta_0$, the local stress balance leads to $\tau_0 = f_0 + \ln \theta_0$. Furthermore, the integral of the stress transfers related to the slip distribution δ on the real line vanishes. Finally, assuming that the pore pressure remains small compared to the lithostatic pressure $p << 1$ (see figure A.8(c,f,i)), this latter expression could be simplified to:

$$\alpha \int_{-\infty}^{+\infty} \ln v dx + \int_{-\infty}^{+\infty} \ln \theta dx = 2 L_0 \ln \theta_0 + f_0 \int_{-\infty}^{+\infty} p dx, \tag{A.30}$$

where L_0 is the half length of the fault initially stressed. Concerning the integral of p on the real line, lets consider the diffusion equation governing the evolution

of pore pressure:

$$\frac{\partial p}{\partial t} = D\frac{\partial^2 p}{\partial x^2} + 2qD\delta_D(x), \tag{A.31}$$

where δ_D is the Dirac delta function. Integrating the diffusion equation on the real line, leads to:

$$\frac{\partial}{\partial t}\int_{-\infty}^{+\infty} p dx = 2qD, \tag{A.32}$$

since p and its space derivatives are supposed to vanish at infinity. We finally end-up with:

$$\int_{-\infty}^{+\infty} p dx = 2qDt. \tag{A.33}$$

The right hand side of the stress balance could be further simplified, assuming that the frictional stress is at steady-state at v_m on the crack, close to the initial stress outside. Accounting for the shape of the slip-rate profiles represented in figures A.9(b) and A.10(b) we have, to the first order:

$$\begin{cases} \alpha \int_{-\infty}^{+\infty} \ln v dx + \int_{-\infty}^{+\infty} \ln\theta dx \\ \simeq (\alpha-1)\int_{-L(t)}^{+L(t)} \ln v_m dx + \left(\int_{-L_0}^{-L} + \int_{L}^{L_0}\right) \ln\theta_0 dx \\ \simeq 2L(t)\ln v_m(t) + 2(L_0 - L(t))\ln\theta_0. \end{cases} \tag{A.34}$$

The stress balance therefore leads to a second equation relating $L(t)$ and $v_m(t)$:

$$(\alpha-1)L(t)\left[\ln v_m(t) - \frac{\ln\theta_0}{\alpha-1}\right] = f_0 qDt. \tag{A.35}$$

Note that this stress balance and the following developments become valid when the left hand side is positive, that is when the maximum slip rate exceeds the limit slip rate $v_l = \theta_0^{1/(\alpha-1)}$. v_l has been defined in the previous sections (equation (17)) as the maximum possible slip rate for accelerated crack propagation. During the expansion phase, v_m seems to increase as the logarithm of time, while $L(t)$ increases much faster, approximately linearly in time, as shown in figures 2(e,f), 3, A.9(c-d) and A.10(c-d). The variation of $\ln v_m$ in equation (A.35) could therefore be neglected, and $\ln v_m$ could be replaced by a constant

λ providing the order of magnitude of the maximum log slip rate. This way, the linear increase of $L(t)$ with time could be retrieved from equation (A.35):

$$L(t) = v_r t = \frac{f_0 q D}{\lambda(\alpha - 1) - \ln \theta_0} t, \tag{A.36}$$

where v_r is an (approximately) constant slip front (rupture) speed. Similarly, the logarithmic increase of v_m with time could be obtained by re-injecting equation (A.36) into expression (A.27), so that we get:

$$v_m(t) = c\left(1 + \ln\sqrt{\frac{t}{t_s}}\right), \qquad c = \frac{4 f_0 q D}{\pi}, \qquad t_s = 4\frac{\lambda^2(\alpha-1)^2 - \ln\theta_0{}^2}{f_0^2 q^2 D}. \tag{A.37}$$

As illustrated in figures A.9(c,d) and A.10(c,d), equations (A.36) and (A.37) provide good approximations to the slip front position and the maximum slip rate obtained numerically.

References

Abercrombie, R.E., 1995. Earthquake source scaling relationships from- 1 to 5 ml using seismograms recorded at 2.5-km depth. Journal of Geophysical Research: Solid Earth 100, 24015–24036.

Ágústsdóttir, T., Woods, J., Greenfield, T., Green, R.G., White, R.S., Winder, T., Brandsdóttir, B., Steinthórsson, S., Soosalu, H., 2016. Strike-slip faulting during the 2014 bárdarbunga-holuhraun dike intrusion, central iceland. Geophysical Research Letters 43, 1495–1503.

Allmann, B.P., Shearer, P.M., 2009. Global variations of stress drop for moderate to large earthquakes. Journal of Geophysical Research: Solid Earth 114.

Ampuero, J., Rubin, A., 2008. Earthquake nucleation on rate and state faults: Aging and slip laws. J. Geophys. Res 113, B01302.

Azad, M., Garagash, D., Satish, M., 2017. Nucleation of dynamic slip on a hydraulically fractured fault. Journal of Geophysical Research: Solid Earth 122, 2812–2830.

Bhattacharya, P., Viesca, R.C., 2019. Fluid-induced aseismic fault slip outpaces pore-fluid migration. Science 364, 464–468.

Bourouis, S., Bernard, P., 2007. Evidence for coupled seismic and aseismic fault slip during water injection in the geothermal site of soultz (france), and implications for seismogenic transients. Geophysical Journal International 169, 723–732.

Cappa, F., Guglielmi, Y., Nussbaum, C., Birkholzer, J., 2018. On the relationship between fault permeability increases, induced stress perturbation, and the growth of aseismic slip during fluid injection. Geophysical Research Letters .

Cochard, A., Rice, J.R., 1997. A spectral method for numerical elastodynamic fracture analysis without spatial replication of the rupture event. Journal of the Mechanics and Physics of Solids 45, 1393–1418.

Cornet, F., Helm, J., Poitrenaud, H., Etchecopar, A., 1997. Seismic and aseismic slips induced by large-scale fluid injections, in: Seismicity associated with mines, reservoirs and fluid injections. Springer, pp. 563–583.

Cornet, F.H., 2016. Seismic and aseismic motions generated by fluid injections. Geomechanics for Energy and the Environment 5, 42–54.

Deichmann, N., Giardini, D., 2009. Earthquakes induced by the stimulation of an enhanced geothermal system below basel (switzerland). Seismological Research Letters 80, 784–798.

Dieterich, J.H., 1979. Modeling of rock friction-1. experimental results and constitutive equations. J. Geophys. Res. *84*, 2161–2168.

Dublanchet, P., 2017. The dynamics of earthquake precursors controlled by effective friction. Geophysical Journal International 212, 853–871.

Dublanchet, P., Bernard, P., Favreau, P., 2013. Creep modulation of omori law generated by a coulomb stress perturbation in a 3-d rate-and-state asperity model. Journal of Geophysical Research: Solid Earth 118, 4774–4793.

Duboeuf, L., De Barros, L., Cappa, F., Guglielmi, Y., Deschamps, A., Seguy, S., 2017. Aseismic motions drive a sparse seismicity during fluid injections into a fractured zone in a carbonate reservoir. Journal of Geophysical Research: Solid Earth 122, 8285–8304.

Duverger, C., Godano, M., Bernard, P., Lyon-Caen, H., Lambotte, S., 2015. The 2003–2004 seismic swarm in the western corinth rift: Evidence for a multiscale pore pressure diffusion process along a permeable fault system. Geophysical Research Letters 42, 7374–7382.

Ellsworth, W.L., 2013. Injection-induced earthquakes. Science 341, 1225942.

Fehlberg, E., 1969. Low-order classical runge-kutta formulas with stepsize control and their application to some heat transfer problems .

Freund, L.B., 1998. Dynamic fracture mechanics. Cambridge university press.

Garagash, D.I., Germanovich, L.N., 2012. Nucleation and arrest of dynamic slip on a pressurized fault. Journal of Geophysical Research: Solid Earth 117.

Ghosh, A., Vidale, J.E., Sweet, J.R., Creager, K.C., Wech, A.G., Houston, H., 2010. Tremor bands sweep cascadia. Geophysical Research Letters 37.

Goodfellow, S., Nasseri, M., Maxwell, S., Young, R., 2015. Hydraulic fracture energy budget: Insights from the laboratory. Geophysical Research Letters 42, 3179–3187.

Guglielmi, Y., Cappa, F., Avouac, J.P., Henry, P., Elsworth, D., 2015. Seismicity triggered by fluid injection–induced aseismic slip. Science 348, 1224–1226.

Gupta, H., Narain, H., Rastogi, B., Mohan, I., 1969. A study of the koyna earthquake of december 10, 1967. Bulletin of the Seismological Society of America 59, 1149–1162.

Hainzl, S., Kraft, T., Wassermann, J., Igel, H., Schmedes, E., 2006. Evidence for rainfall-triggered earthquake activity. Geophysical Research Letters 33.

Helmstetter, A., Shaw, B.E., 2009. Afterslip and aftershocks in the rate-and-state friction law. Journal of Geophysical Research: Solid Earth 114.

Houston, H., Delbridge, B.G., Wech, A.G., Creager, K.C., 2011. Rapid tremor reversals in cascadia generated by a weakened plate interface. Nature Geoscience 4, 404.

Jaeger, J.C., Cook, N.G., Zimmerman, R., 2009. Fundamentals of rock mechanics. John Wiley & Sons.

Jolivet, R., Lasserre, C., Doin, M.P., Peltzer, G., Avouac, J.P., Sun, J., Dailu, R., 2013. Spatio-temporal evolution of aseismic slip along the haiyuan fault, china: Implications for fault frictional properties. Earth and Planetary Science Letters 377, 23–33.

King, F.W., 2009. Hilbert transforms. vol. 1, volume 124 of encyclopedia of mathematics and its applications.

Lengliné, O., Boubacar, M., Schmittbuhl, J., 2017. Seismicity related to the hydraulic stimulation of grt1, rittershoffen, france. Geophysical Journal International 208, 1704–1715.

Marone, C., 1998. Laboratory-derived friction laws and their application to seismic faulting. Annual Review of Earth and Planetary Sciences 26, 643–696.

Marone, C.J., Scholtz, C., Bilham, R., 1991. On the mechanics of earthquake afterslip. Journal of Geophysical Research: Solid Earth 96, 8441–8452.

Perfettini, H., Ampuero, J., 2008. Dynamics of a velocity strengthening fault region: Implications for slow earthquakes and postseismic slip. J. Geophys. Res 113, B09411.

Perfettini, H., Avouac, J., 2004. Postseismic relaxation driven by brittle creep: A possible mechanism to reconcile geodetic measurements and the decay rate of aftershocks, application to the chi-chi earthquake, taiwan. J. Geophys. Res 109.

Rice, J.R., 2006. Heating and weakening of faults during earthquake slip. Journal of Geophysical Research: Solid Earth 111.

Roland, E., McGuire, J.J., 2009. Earthquake swarms on transform faults. Geophysical Journal International 178, 1677–1690.

Rubin, A., Ampuero, J., 2005. Earthquake nucleation on (aging) rate and state faults. J. Geophys. Res 110, B11312.

Rubin, A.M., Ampuero, J.P., 2009. Self-similar slip pulses during rate-and-state earthquake nucleation. Journal of Geophysical Research: Solid Earth 114.

Ruina, A.L., 1983. Slip instability and state variable friction laws. J. Geophys. Res. *88*, 10,359–10,370.

Schaff, D., Beroza, G., Shaw, B., 1998. Postseismic response of repeating aftershocks. Geophys. Res. Lett 25, 4549–4552.

Temme, N., 2010. Error functions, dawsons and fresnel integrals. NIST handbook of mathematical functions , 159–171.

Turcotte, D., Schubert, G., 2014. Geodynamics. Cambridge university press.

Wei, S., Avouac, J.P., Hudnut, K.W., Donnellan, A., Parker, J.W., Graves, R.W., Helmberger, D., Fielding, E., Liu, Z., Cappa, F., et al., 2015. The 2012 brawley swarm triggered by injection-induced aseismic slip. Earth and Planetary Science Letters 422, 115–125.